Mixed Dimethylammonium/Methylammonium Lead Halide Perovskite Single Crystals for Improved Structural Stability and Enhanced Photodetection

Aniruddha Ray,[1,2] *Beatriz Martín-García,*[1,3]*Anna Moliterni,*[4,*] *Nicola Casati,*[5] *Karunakara Moorthy Boopathi,*[1] *Davide Spirito,*[6] *Luca Goldoni,*[1] *Mirko Prato,*[1] *Carlotta Giacobbe,*[7] *Cinzia Giannini,*[3] *Francesco Di Stasio,*[1] *Roman Krahne,*[1,*] *Liberato Manna,*[1,*] *Ahmed L. Abdelhady*[1,8*]

[1]Istituto Italiano di Tecnologia, Via Morego 30, 16163 Genova, Italy

[2]Dipartimento di Chimica e Chimica Industriale, Università degli Studi di Genova, Via Dodecaneso 31, 16146 Genova, Italy

[3]CIC nanoGUNE, Tolosa Hiribidea, 76, 20018 Donostia-San Sebastian, Spain

[4]Istituto di Cristallografia, Consiglio Nazionale delle Ricerche, Via Amendola 122/O, 70126 Bari, Italy

[5]Laboratory for Synchrotron Radiation—Condensed Matter, Paul Scherrer Institut, 5232 Villigen, Switzerland

[6]IHP—Leibniz-Institut für innovative Mikroelektronik, Im Technologiepark 25, D-15236 Frankfurt (Oder), Germany

[7]European Synchrotron Radiation Facility, 71 Avenue Des Martyrs, Grenoble 38040, France

[8]ŁUKASIEWICZ Research Network PORT-Polish Center for Technology Development, ul. Stabłowicka 147, 54-066 Wrocław, Poland

*Corresponding author(s): annagrazia.moliterni@ic.cnr.it, roman.krahne@iit.it, liberato.manna@iit.it and ahmed.abdelhady@iit.it

Keywords: perovskite, single crystals, dimethylammonium, photodetectors, temperature-dependent properties

We utilize the solvent acidolysis crystallization technique to grow mixed dimethylammonium/methylammonium lead tribromide (DMA/$MAPbBr_3$) crystals reaching the highest dimethylammonium incorporation of 44% while maintaining the 3D cubic perovskite phase. These mixed perovskite crystals show suppression of the orthorhombic phase and a lower tetragonal to cubic phase transition temperature compared to $MAPbBr_3$. We observe distinct behavior in the temperature-dependent photoluminescence properties of $MAPbBr_3$ and mixed DMA/$MAPbBr_3$ crystals due to the different organic cation dynamics governing the phase transition(s). Furthermore, we fabricate lateral photodetectors which show that, at room temperature, the mixed crystals possess higher detectivity compared to $MAPbBr_3$ crystals caused by structural compression and reduced surface trap density. Remarkably, the mixed crystal devices exhibit large enhancement in their detectivity below the phase transition temperature (at 200K), while the $MAPbBr_3$ devices demonstrate insignificant changes. The higher detectivity makes our devices attractive for visible light communication and for space applications. Our results highlight the importance of the synthetic technique for the halide perovskites compositional engineering that governs their structural and optoelectronic properties.

1. Introduction

Halide perovskites with the general formula AMX_3 (A = methylammonium – MA, formamidinium – FA, or Cs, M = Pb^{2+} or Sn^{2+}, and X = Cl^-, Br^-, or I^-)[1,2] have been, over the last few years, intensively investigated for photodetection applications.[3–7] Though the A-site organic cation does not participate in the band edge states, it significantly influences the room temperature (RT) optical properties indirectly through changes to the structure of the octahedra lattice. For example, increasing the size of the A-site cation from Cs^+ to MA^+ to FA^+ narrows the bandgap due to decreased octahedral tilting.[8,9] Furthermore, cryogenic studies have demonstrated that the A-site cation also impacts the temperature-dependent optical[10–17] and structural properties.[14,15,18–24] Temperature-dependent neutron/X-ray diffraction and photoluminescence (PL) measurements on $MAPbBr_3$ revealed that the MA cation transformation from an ordered to a disordered state is correlated with an increased integrated PL intensity, and is also suggested to induce the orthorhombic to tetragonal phase transition.[14,25] Also, temperature-dependent Raman spectroscopy identified that hydrogen bonding between MA and Br controls the MA cation dynamics and subsequently the inorganic octahedra tilting.[15]

The research spotlight is now shifting to mixed organic cations in which a larger A-site organic cation such as ethylenediammonium (EN),[26] guanidinium (GUA),[27] or dimethylammonium (DMA)[28] is incorporated into the perovskite structure. In particular, DMA as an A-site cation has recently been discovered to have been unintentionally incorporated in the perovskite composition as a side effect in specific synthetic routes involving the use of acids, highlighting the significant role of the synthetic method in the extent of A-site cation incorporation.[29] To date, the deliberate substitution of MA with DMA in both Br- and I-based perovskites has achieved only up to 15-28% DMA incorporation,[30–32] with more DMA leading to mixed phases containing segregated non-perovskite $DMAPbX_3$. Specifically, in the case of the Br-based compositions, the pure perovskite framework is found to be maintained only up to 23% DMA incorporation.[28] A blue shift in optical features upon incorporating DMA in mixed $(FA/Cs)PbBr_3$ has been related to an anomalous octahedral tilting[33] and not to the expected lattice volume expansion. Interestingly, in $MAPbBr_3$, when increasing amounts of MA were replaced with DMA, the phase transitions were found to first occur at lower temperatures (4% DMA), and then were completely suppressed (21% DMA) due to the lattice deformation leading to reduced interactions between the molecular cations.[20] However, higher DMA containing phases were not studied as it was suggested in a previous study that it led to phase segregation.[28]

Here, we explore the role of incorporating a large amount of the DMA cation in $MAPbBr_3$ crystals on the temperature-dependent structural and optical properties, and the performance of photodetectors based on this heavily DMA-substituted perovskite. The crystals were grown using the solvent acidolysis crystallization that we previously reported for $MAPbX_3$ crystals[34,35] and also for Pb-free crystals.[36] We managed to incorporate up to 44% DMA, which is higher than the reported solubility limit of DMA in $MAPbX_3$ perovskites,[28,30–32] while maintaining the three-dimensional (3D) cubic perovskite structure, with no sign of the non-perovskite $DMAPbBr_3$. Temperature-dependent synchrotron X-ray powder diffraction and temperature-dependent micro-Raman measurements, in the range 80 – 300 K, showed a lowered cubic to tetragonal phase transition temperature and the absence of the orthorhombic phase in DMA/$MAPbBr_3$, compared to pure $MAPbBr_3$. This behavior is confirmed by the intensity of the high energy PL peak of the mixed crystals that displayed a trend with increasing DMA% that suggests a gradual lowering in the tetragonal to cubic phase transition temperature. We fabricated lateral photodetectors in which, at RT, the mixed crystal devices possessed around 2 times higher detectivity (D) compared to the $MAPbBr_3$ devices due to reduced surface trap density. Remarkably, in their tetragonal phase (at 200 K), the mixed crystals displayed more than 3 times enhancement in their D compared to $MAPbBr_3$ crystals. Furthermore, the 44% DMA devices demonstrated higher stability with respect to the pure MA devices when tested after 1 week.

2. Results and discussion

The mm-sized crystals were grown using a modified solvent acidolysis crystallization (SAC) protocol that we previously reported for $MAPbX_3$ crystals[34,35] and also for Pb-free crystals.[36] The crystallization schematics and the as-grown crystals of $MAPbBr_3$ and DMA/$MAPbBr_3$ are shown in Figure S1 (Supporting Information). For quantitative analysis, we performed proton nuclear magnetic resonance (^{1}H NMR) analysis on the mixed crystals, as displayed in Figure

S2a, and we were able to assign specifically the signal from the DMA and MA cations. Subsequently, the molar ratio was inferred from each integrated peak intensity, normalized to the protons generating the signal (6 protons for DMA and 3 protons for MA), and the DMA% in the crystals was found to be around 44%. This DMA content is higher than any previously reported value in DMA/MAPbX$_3$ while maintaining the 3D cubic phase and without any signals corresponding to the non-perovskite phase, as discussed below.[28,30–32] The DMA content can be controlled by varying the DMF:NMF ratio in the feed solution. For instance, we grew crystals with 17% and 26% DMA by lowering the DMF:NMF ratio (Figure S2b,c). However, a higher DMF:NMF ratio in the feed solution resulted in clear impurity diffraction peaks (Figure S3), suggesting that 44% DMA incorporation could be the highest alloying level using the SAC process. Hereafter, the three DMA/MA mixed crystals with a 3D perovskite structure will be referred to as 17% DMA, 26% DMA, and 44% DMA. Regarding the Br:Pb ratio, even the 44% DMA crystals were very similar to the pure MA crystals, based on energy-dispersive X-ray spectroscopy (EDS) analysis (Table S1).

The as-grown 44% DMA mixed crystals have been preliminary investigated by X-ray powder diffraction (XRPD), with a laboratory equipment. The obtained diffraction pattern is very similar to the pure MA pattern, which can be indexed to the cubic phase ICSD 268785, and no diffraction peaks corresponding to the non-perovskite DMAPbBr$_3$ phase are detected, confirming that the 3D cubic structure is maintained **(Figure 1(a))**. The difference between the pure MA and the 44% DMA crystals diffraction patterns is manifested in the (expected) shift to lower Bragg angles, as shown in **Figure 1(b)** due to the incorporation of the larger organic cation (DMA) leading to the observed lattice expansion.[20,28,33] An additional lattice expansion is recorded upon grinding the 44% DMA mixed crystals, which does not occur for the pure MA crystals (**Figure 1(c)**), indicating that the mixed crystals are structurally compressed. Lattice compression has been previously reported to enhance the optoelectronic properties since it leads to the removal of mid-bandgap trap states and shallower trap states[37–39] and therefore is beneficial for photodetection, in particular, in terms of detectivity (D).[35,40] Diffraction patterns of the ground 17% and 26% DMA crystals are shown in Figure S4, evidencing peaks at intermediate positions between those of pure MA and 44% DMA.

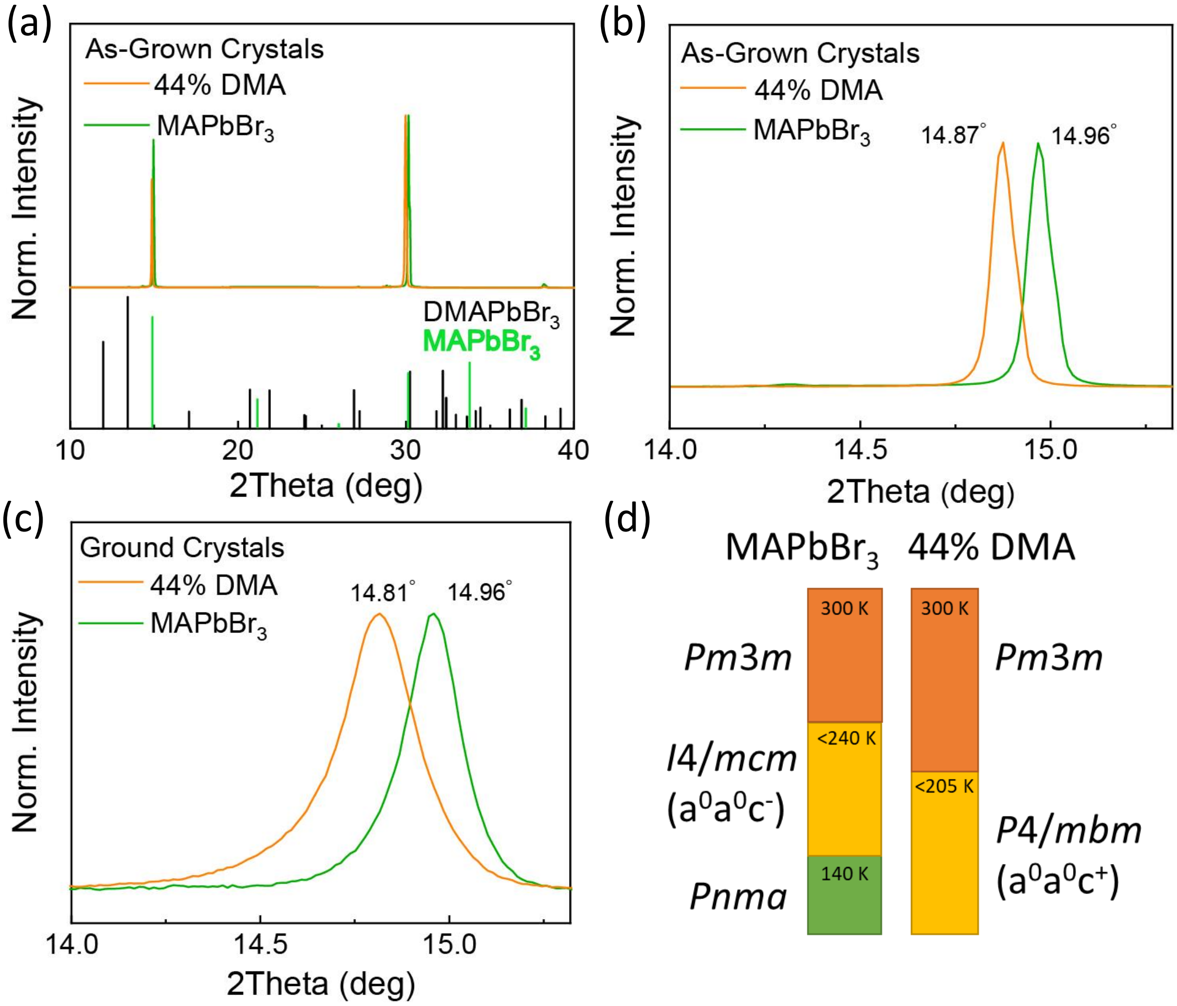

Figure 1. (a) XRPD patterns of $MAPbBr_3$ and 44% DMA compared to the cubic $MAPbBr_3$ (ICSD 268785) and the non-perovskite $DMAPbBr_3$ phase (ICSD 402591), and zoomed in (001) peak of (b) as-grown crystals and (c) ground crystals. (d) Illustration of the temperature-dependent phases in both samples; dark orange = cubic, light orange = tetragonal, and green = orthorhombic.

Temperature-dependent synchrotron radiation X-ray powder diffraction (SXRPD) data were collected in the range 80 K - 300 K on the pure MA and the 44% DMA samples. Crystalline phase, unit cell volume, and Pb-Br-Pb angle at selected temperatures are summarized in **Table 1**; the lattice parameters are reported in Table S2. For details on SXRPD data processing see Note S1 and accompanied Figures S5-6. The results for the pure MA powders confirmed the previously reported data;[14,41] $MAPbBr_3$ remains cubic from room temperature to 240 K and below this temperature a cubic to tetragonal phase transition occurs, which is followed by a tetragonal to orthorhombic phase transition around 160 K. On the other hand, the 44% DMA sample demonstrated a reduced cubic to tetragonal phase transition temperature ($\approx$205 K instead of $\approx$240 K) and no orthorhombic phase was recorded down to 80 K. **Figure 1(d)** shows the temperature ranges of the phases in both samples. The cubic to tetragonal phase transition that we observe for the DMA/MA crystals is not in line with a recent work that reported a completely suppressed phase transition, where the cubic phase was maintained down to temperatures of 100 K, even with only 21% DMA.[20] Mixed A-site cations have been previously reported to suppress phase transitions, however, through incorporating the smaller-sized Cs cation in $MAPbBr_3$ and $FAPbBr_3$, and this was attributed to compressive chemical pressure.[42,43] In this work, we propose that, due to the probable greater disorder of the organic cations in the 44% DMA sample, a higher symmetry and less distorted inorganic framework is realized compared to the pure $MAPbBr_3$ sample at a given temperature. This is based on the following points: (i) the difficulties presented in locating the organic cation, even at the lowest temperatures, in the case of the 44% DMA sample, and (ii) the symmetry of the 44% DMA being larger than orthorhombic even at T = 80 K. Furthermore, our proposal is consolidated by the outcomes of the Yang *et al*. investigation[14] on the order-disorder transformation of MA, in which they related increasing organic cation disorder ocurring at increased temperatures to the occurrence of a transition to a higher symmetry phase.

In terms of Pb-Br-Pb angles that govern the octahedral tilt, the pure MA sample showed no distortion in the cubic phase. Upon phase transition, an in-plane distortion was detected in the tetragonal phase and both in-plane and out-of-plane distortions were recorded for the orthorhombic phase. Similarly, in-plane distortions were recorded in the tetragonal phase of the mixed DMA/MAPbBr$_3$ (see Table 1). This indicates that, at RT, the main difference between the pure MA and the 44% DMA samples lies in the observed cell volume expansion (≈2.63%) due to the incorporation of the larger DMA cations.

Table 1. Crystal phase, cell volume, and Pb-Br-Pb angle of MAPbBr$_3$ and 44% DMA at selected temperatures (T).

	MAPbBr$_3$			**Mixed DMA/MAPbBr$_3$**		
T (K)	**Phase**	**Cell volume (Å^3)**	**Pb-Br-Pb angle (°) In-plane Out-of-plane**	**Phase**	**Cell volume (Å^3)**	**Pb-Br-Pb angle (°) In-plane Out-of-plane**
300	Cubic	208.504(4)	180 180	Cubic	213.995(14)	180 180
240	Cubic	206.964(4)	180 180	Cubic	212.395(16)	180 180
220	Tetragonal	826.13(6)	168.25 180	Cubic	211.864(15)	180 180
205	Tetragonal	825.02(5)	165.68 180	Cubic	211.425(14)	180 180
200	Tetragonal	824.75(6)	165.23 180	Tetragonal	421.99(15)	170.90 180
180	Tetragonal	822.91(6)	164.60 180	Tetragonal	420.67(14)	167.54 180
160	Tetragonal	821.46(6)	162.76 180	Tetragonal	419.56(10)	166.09 180
140	Orthorhombic	814.01(3)	159.44 172.14	Tetragonal	418.13(11)	165.19 180
120	Orthorhombic	811.54(3)	157.88 170.90	Tetragonal	417.23(12)	164.56 180
80	Orthorhombic	810.61(14)	157.56 170.32	Tetragonal	415.09(11)	164.56 180

In the case of the mixed 44% DMA, the indexing program *N-TREOR09*[44] indicates, as one of the most plausible cells, a half volume tetragonal cell, whose *a*-axis is similar to that one of the pure sample, while the *c*-axis is nearly halved (see Table S2). When this tetragonal cell is used in the next steps of the structure solution process, *EXPO2014* suggests the space group *P*4/*mbm* as the most plausible space group for the mixed sample (in the case of pure $MAPbBr_3$ the most plausible space group is *I*4/*mcm*). The two space groups *P*4/*mbm* and *I*4/*mcm* are typical of tetragonal halide perovskites.[45] These space groups are in line with the recorded large compression in the *c*-axis where *P*4/*mbm* and *I*4/*mcm* are characterized with unit cell parameters of $a = b \approx \sqrt{2}a_c$ and $c = a_c$ and $a = b \approx \sqrt{2}a_c$ and $c = 2a_c$ (a_c is the lattice constant in the cubic phase), respectively, leading to doubling of the pure $MAPbBr_3$ cell's volume compared to the mixed sample as noted in Table 1.[45,46] The main difference between the *P*4/*mbm* and *I*4/*mcm* is in the octahedral tilt. In the former, neighbouring octahedra along the *c*-axis rotate in the same direction, while in the latter they rotate in the opposite direction.[45,47] A similar change in the octahedral tilting preference was also previously observed in $MA_{1-x}Cs_xPbBr_3$, when $0.2 < x \leq 0.4$.[43] It is expected that the different adopted tetragonal unit cells are due to the difference in hydrogen-bonding between the organic cations (MA and DMA) and the inorganic framework.[48]

The successful incorporation of the DMA cation in the crystals is also confirmed by micro-Raman spectroscopy at room temperature (RT). In the mixed crystals, we observe additional Raman modes (Figure S7(a)) at 890 cm^{-1}, 1350 cm$^{-1,}$ and 1461 cm^{-1} corresponding to the C-N-C stretching, CH_3 rocking, and CH_3 bending modes of the DMA cation, respectively.[20,49] Indeed, it is possible to observe the progressive increase of the DMA cation concentration in the crystal by evaluating the integrated area of the DMA mode at ~890 cm^{-1} with respect to the MA mode at ~968 cm^{-1}. We found a linear trend between the integrated area ratio and the DMA cation concentration, by using the quantitative data from the NMR analysis for the latter (Figure

S7(b)). Moreover, the coexistence of DMA and MA promotes a shift in the position of some of the vibrational modes, as highlighted for example for the red shift of the 1592 cm^{-1} peak corresponding to the N-H asymmetric bending mode (NH_3^+ in MA) (Figure S7(c)) to 1586 cm^{-1} at the highest DMA concentration (44%), indicating a stronger $H_N\cdots Br$ bonding for the MA cations in the mixed crystals compared to in the pure MA crystals.

In order to gain insights into the rearrangement of the organic cation(s) during the phase transitions, we carried out temperature-dependent micro-Raman spectroscopy measurements between 90 K and 313 K.[15,50] In **Figure 2**, we focus on the vibrational modes that are more closely related to $H_C\cdots Br$ and $H_N\cdots Br$ bonding, and therefore, more sensitive to the reorganization of the MA cations in the pure MA and 44% DMA crystals during the phase transitions, i.e., C-H, N-H, and C-N stretching modes of MA (see Figure S8 for the 17% and 26% DMA samples). In the orthorhombic phase of the MA crystals ($T < 143$ K), the corresponding NH_3^+ and CH_3 vibrational modes[15,41,51] are sharp and narrow, indicating high ordering and locked MA cations.[15,51] The peak position and linewidth values of the stretching modes of MA at T = 93 K in all crystals (Table S3) highlight that the orthorhombic phase in all three mixed crystals is not reached, which is in line with the SXRPD results in the case of the 44% DMA sample. Note that, when passing from the tetragonal to the cubic phase, in all cases, there is only a subtle change in the MA Raman modes. On the other hand, the DMA Raman modes **(Figure 3**, see Figure S9 for the 16% and 27% DMA samples**)** around 1014 cm^{-1}, and 1075 cm^{-1} exhibit a gradual shift in full width half maxima (FWHM) around 210 K that occurs close to the cubic to tetragonal phase transition recorded from the SXRPD measurements for the 44% DMA sample.

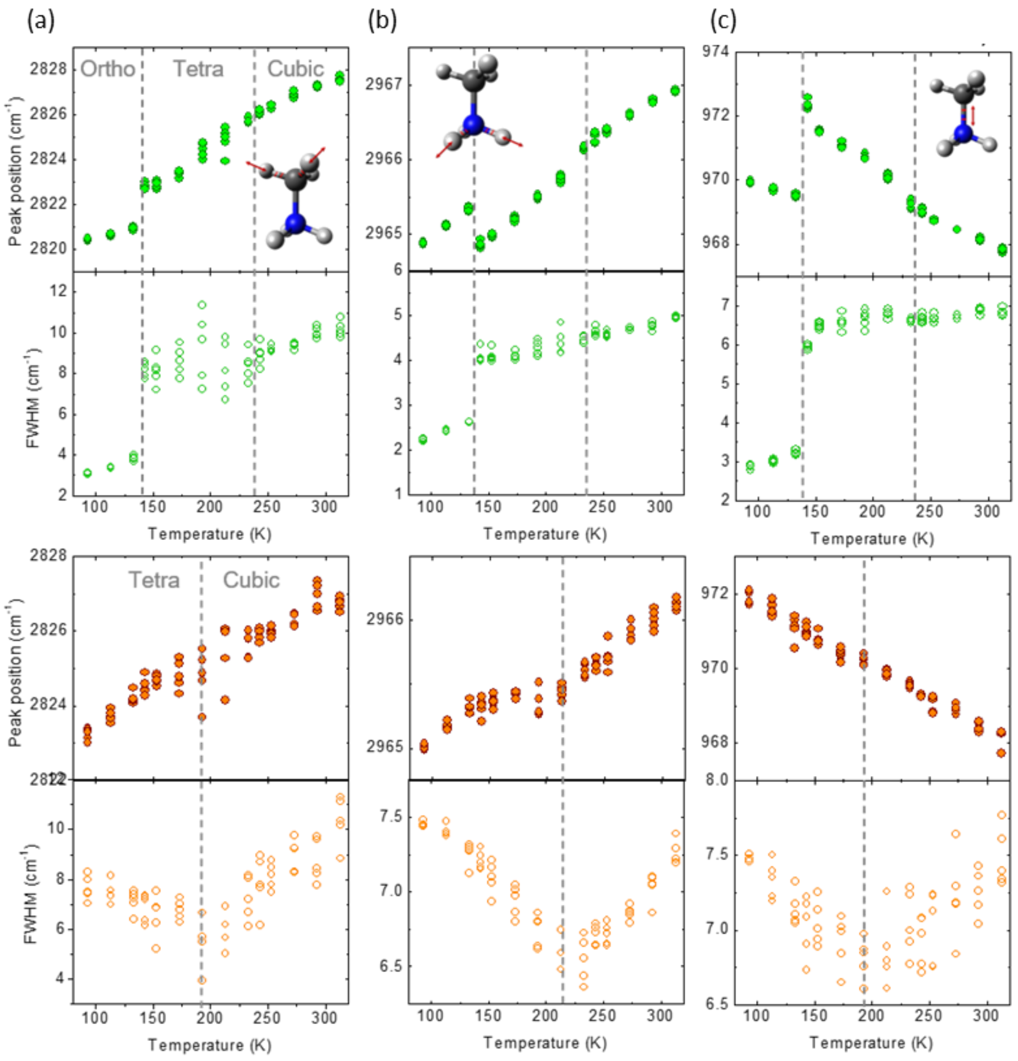

Figure 2. Evolution of the C-H, N-H, and C-N stretching modes of MA [15,41,51] in terms of Raman shift (peak position) and linewidth (FWHM) as a function of temperature in both crystals: $MAPbBr_3$ (green) and 44% DMA (orange) crystals. The dotted lines mark the phase transition temperatures. Sketches of the vibration modes[15,51] drawn with Avogadro software[52] are shown as insets. The results shown are from five different points in each sample.

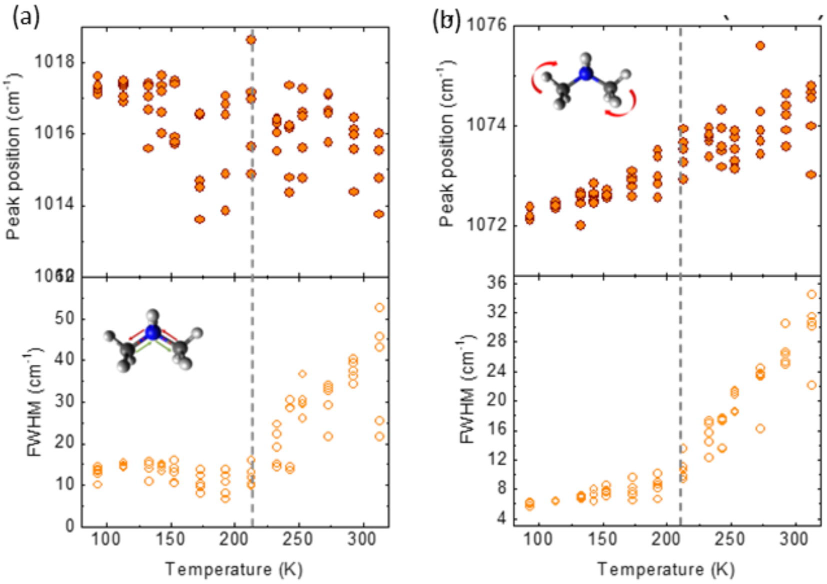

Figure 3. Evolution of the C-N-C stretching and rocking modes of DMA [20,49] in terms of Raman shift (peak position) and linewidth (FWHM) as a function of temperature in the 44% DMA crystals. The dotted lines mark the phase transition temperatures. Sketches of the vibration modes drawn with Avogadro software[52] are shown as insets. The results shown are from five different points in each sample.

We next discuss the band structure of the pure MA and the 44% DMA crystals, and start with ultraviolet photoemission spectroscopy (UPS) measurements to obtain the energy level of the valence band maxima (VBM). Both the pure MA and the 44% DMA crystals possess very similar VBM values of 5.8 eV and 5.7 eV, respectively (Figure S10a,b). We also measured the absorbance spectra of both crystals (Figure S10c), which exhibit a bandgap widening in the case of the mixed 44% DMA due to the lattice expansion (see Table 1), unlike what has been previously reported and attributed to the increased octahedral tilting.[33] Based on these measurements, the band structure of both crystals is represented in Figure S10d.

We also performed temperature-dependent PL studies on all crystals in the range from 80 to 300 K. As shown in **Figure 4(a,b)** (see Figure S11 for semi-log scale plots), in the pure MA and the 44% DMA crystals, three Voigt-shaped peaks (**Figure 4(c,d)**) are required to fit the emission spectra. In the case of the pure MA crystals, the three peaks are a high-energy (HE) peak, a low-energy (LE) peak, and a third broad peak around 2.1 eV that is only present at lower temperatures (80 – 120 K), i.e. below the tetragonal to orthorhombic phase transition, and which is strongly red-shifted from HE and LE peaks. Several reports have attributed this peak to sub-bandgap trap states due to structural or compositional disorder at low temperatures leading to trap-assisted emission.[10–13] In the case of the 44% DMA crystals, three PL peaks, instead, are detected at all temperatures. Here in addition to the HE and LE peaks, a third peak that is energetically close to the LE peak is present. The absence of the energetically shifted broad PL peak in the mixed crystals indicates reduced sub-bandgap states at low temperatures compared to the pure MA crystals. For the temperature-dependent PL results on the 17% and 26% DMA crystals, see Figure S12.

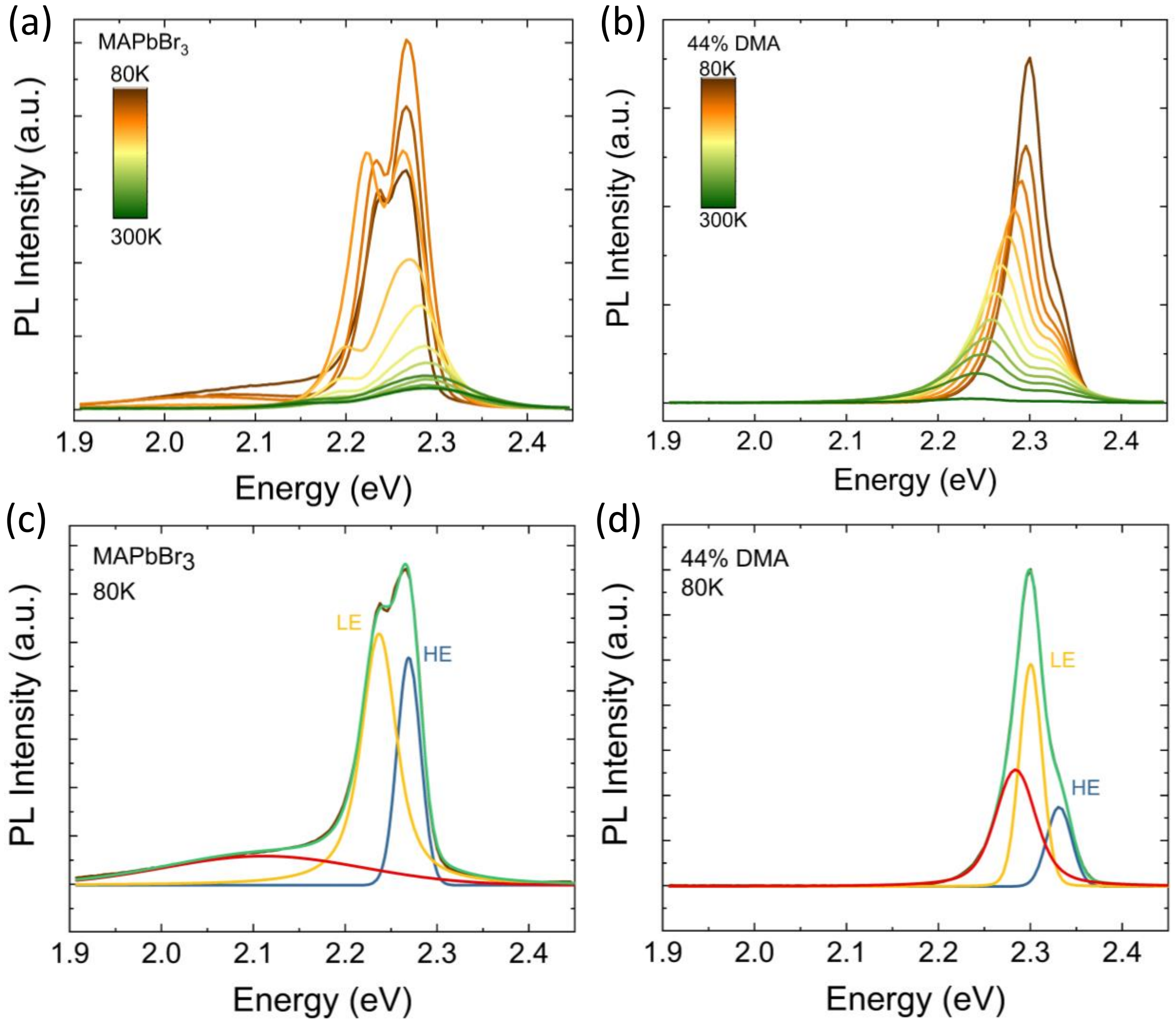

Figure 4. Temperature-dependent PL spectra recorded with laser excitation at 445 nm (2.79 eV) of (a) $MAPbBr_3$ (b) 44% DMA crystal. The fitting with Voigt-shaped peaks of the spectra recorded at 80 K is shown for (c) $MAPbBr_3$ and (d) 44% DMA. Here the spectra are displayed in green, the LE peak in yellow, the HE peak in blue, and the additional third peak in red.

Common to both pure MA and 44% DMA crystals is the presence of the two PL peaks (HE and LE) that have been well documented in literature in the case of the $MAPbBr_3$, but for which the origin of the LE peak is still being debated. The LE peak has been attributed to several different origins, including the coexistence of another structural phase (at low temperature)[10,53–55] and Rashba splitting.[12,56–58] Importantly, the LE peak in our crystals ($MAPbBr_3$ and 44% DMA) displays the same trend as a function of temperature; a pronounced red shift as the temperature increases from 80 K to RT (Figure S13), accounting for the electron–phonon coupling effect,[56,57] or the degree of Rashba splitting.[58] Hence, we focus here on the HE peak (band-to-band peak) for which we observe different trends for the different crystal compositions, as discussed below.

In the case of the pure MA crystals, the HE peak shows a blue shift upon increasing temperature except for around 160 K due to the orthorhombic to tetragonal phase transition[14] **(Figure 5(a))**. This blue shift has been already well documented in the halide perovskite field and is related to thermal expansion of the lattice and stabilization of the valence band maxima.[59–65] In the 44% DMA, the blue shift could be detected in the HE peak only above 180 K (**Figure 5(a)**), that is, close to the tetragonal to cubic phase transition as detected by SXRPD (Table 1). In the tetragonal phase, a red shift is observed with increasing temperature. Increased electron-phonon coupling cannot account for the red shift, as the FWHM of the PL peaks is in fact narrower for the mixed crystal compared to the pure MA crystal (**Figure 5(b)**). Furthermore, it was proposed that a slight red shift in the bandgap due to electron−phonon coupling is evident mainly in small nanocrystals but not in bulk perovskites.[66] Instead, the diverse temperature dependence of the HE PL peak in the 44% DMA crystals could possibly highlight that reduced octahedral tilting, which leads to a redshifted PL, plays a more important role than the thermal expansion of the lattice in the tetragonal mixed crystals. Note that the red shift in the HE PL peak position is also observed in the cases of 17% and 26% DMA at low temperatures (Figure S14a) with their FWHM remaining similar to 44% DMA case (Figure S14b).

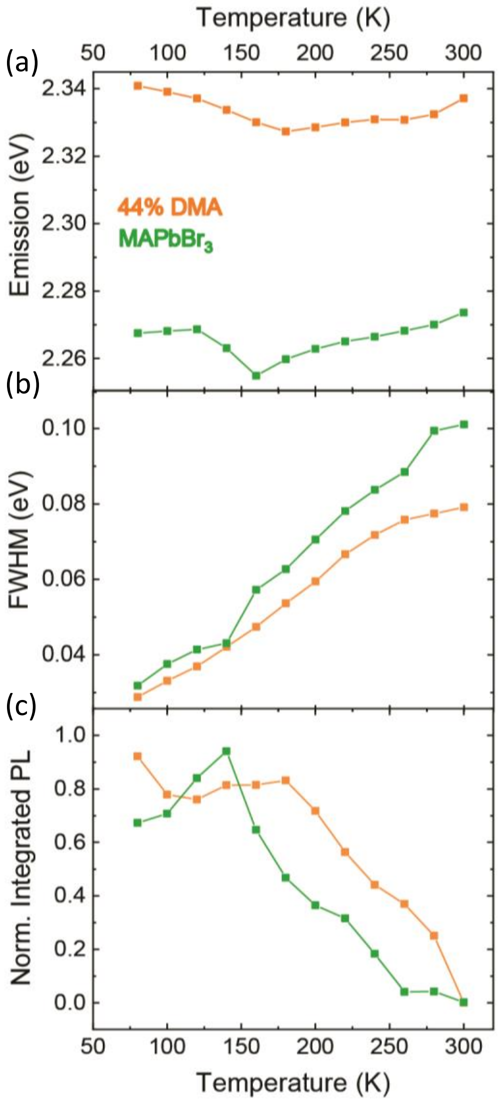

Figure 5. Temperature-dependent evolution of the (a) peak position (b) full width half maxima (FWHM) and (c) integrated PL intensity of the HE peaks of $MAPbBr_3$ (green) and 44% DMA (orange) crystals.

Focusing on the integrated PL intensity of the HE peak, we found that a similar trend is observed for both the pure MA and the 44% DMA crystals, with a temperature range around 120 K to 180 K in which the integrated PL intensity increases with increasing temperature instead of dropping (**Figure 5(c)**). This was previously attributed to various effects, including increased dielectric screening during the transformation of the MA cations from order to disorder starting around 100 K, thus leading to shallower defects and reduced non-radiative recombination.[14] It has also been reported that the reorienting motion of the organic cation(s) provides screening of charge carriers from charged defects.[67,68] However, in the case of our three mixed crystals, we recorded a trend for the temperature at which the HE PL peak intensity is maximized. The 44% DMA peaks at 180 K (**Figure 5(c)**), while the 17% and 26% DMA crystals peak at 240 K and 200 K, respectively (Figure S14). This may indicate that there is a shift in the tetragonal to cubic phase transition temperature with the increase in the DMA%, which affects the integrated PL intensity. This is in line with the work by Oshero et al.[69] in which the highest PL quantum efficiency was recorded around the phase transition temperature. Time-resolved PL (TRPL), monitoring the HE PL peak, revealed that a triexponential fitting is required for all crystals with the longest lifetime recorded for the 17% DMA crystals (Figure S15).

We fabricated lateral photodetectors (Au/perovskite/Au), in which the performance should be dominated by the surface properties of the perovskite crystals, and we compared the photodetector performance at temperatures that correspond to two different crystal structures – cubic at 300 K and tetragonal at 200 K. **Figure 6(a)** shows the spectral detectivity (D) of MA crystals and 44% DMA crystals highlighting that the DMA incorporation results in doubling the D at RT under low bias of 1V. Furthermore, at 200 K, in their tetragonal phases, the D of the 44% DMA devices reach more than 3 times that of the pure MA crystals (**Figure 6(b)**). The lower dark current of the 44% DMA crystals, both at RT and 200 K, indicates that they involve fewer defects compared to the pure crystals (**Figure 6(c,d)**).[4,35] Note that the 44% DMA crystals are structurally compressed, which leads to reduced/shallower traps that are beneficial for photodetection, in particular for the enhancement of D.[35,40] The devices fabricated with 17% and 26% DMA display an intermediate behaviour (Figure S16). In terms of device responsivity (R), the pure MA and the 44% DMA crystals performance are quite similar, in particular at room temperature (Figure S17).

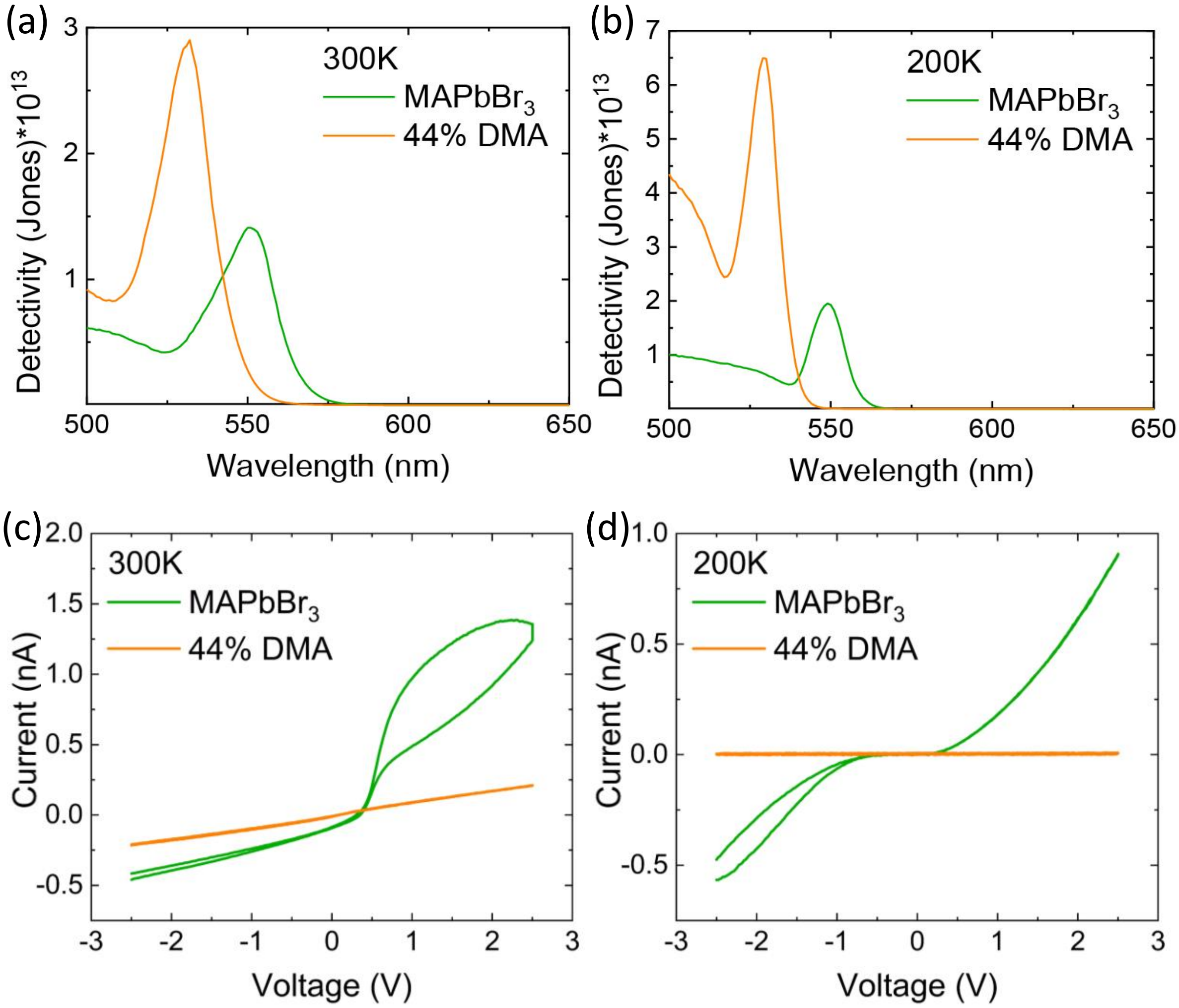

Figure 6. (a and b) Spectral detectivity (D) of MA crystals and 44% DMA crystals at 1V at 300 K and 200 K, respectively, and (c and d) corresponding IV curves under dark conditions.

An important characteristic in halide perovskite optoelectronic devices is the hysteresis that results from ion migration and could be bias polarity dependent.[70] **Figure 6(c,d)** (see Figure

S18 for semi-log scale plots) show IV curves under both forward and reverse biases in lateral devices. In particular, at RT, hysteresis is clearly suppressed in the mixed crystals with respect to the $MAPbBr_3$ crystals, which is in agreement with previous work involving the incorporation of relatively large A-site organic cations.[71] Furthermore, we tested the device performance after one week of storage under nitrogen atmosphere in a glove box, and as could be expected, the incorporation of DMA resulted in higher stability as the D of the 44% DMA devices dropped by 40% compared to the fresh devices (Figure S19). On the other hand, the D of the pure MA crystals dropped by 70%. The higher stability upon the incorporation of DMA has been previously attributed to weaker hydrogen bonding between perovskite and ambient water.[31]

3. Conclusion

Using solvent acidolysis crystallization (SAC), we managed to substitute up to 44% of the MA with DMA while maintaining the cubic perovskite phase, and without any signs of the non-perovskite $DMAPbBr_3$ phase, leading to a suppression of the orthorhombic phase down to 80 K, and a lower cubic to tetragonal phase transition temperature compared to the pure $MAPbBr_3$. We propose that these structural differences are a consequence of the greater disorder of the organic cations in the mixed sample, therefore a higher symmetry and less distorted inorganic framework is realized compared to the pure $MAPbBr_3$ sample at a given temperature. As the DMA% increased, the PL intensity maximized at lower temperatures, suggesting a gradual shift in the temperature of the tetragonal to cubic phase transition. We fabricated lateral photodetectors that demonstrated 2 and more than 3 times enhancement in D, at RT and at 200 K, respectively, for the 44% DMA devices compared to the pure $MAPbBr_3$. This enhancement is attributed to structural compression and reduced surface trap density in the mixed crystals that significantly suppresses the dark current. The enhancement in D at both room temperature and low temperature demonstrate the potential use of the mixed $DMA/MAPbBr_3$ in visible light communication, and in space applications. The results obtained in this study inspire the necessity to explore alternate synthetic techniques while testing the solubility limit of large A-site cations, as incorporating higher fractions can lead to vastly different structural and optoelectronic properties thus opening up a new dimension of material's tunability.

4. Experimental

Materials: Lead bromide ($PbBr_2$, 99%), hydrobromic acid (HBr, 48 wt% in water), *N*-methylformamide (NMF, 99.9%), *N,N*-dimethylformamide (DMF, 99.9%), and dichloromethane (DCM, 99.8%) were purchased from Sigma-Aldrich and used as received.

Crystal growth: Precursor solutions for methylammonium lead tribromide ($MAPbBr_3$) crystals were prepared by dissolving 0.4M $PbBr_2$ in a mixed solvent system consisting of NMF and HBr (5.67:1 by vol). In the case of the mixed dimethylammonium-methylammonium lead tribromide ($DMA/MAPbBr_3$) the same concentration of 0.4M $PbBr_2$ is dissolved in DMF, NMF, and HBr (2.18:3.48:1, 3.14:2.51:1, and 4.05:1.5:1 by vol, for the 17%, 26% and 44% DMA, respectively). Subsequently, 1 ml of the respective precursor solutions was transferred in 8 mL vials and sealed with an aluminium foil, and inserted into a larger 40 mL vial containing 7.5 mL of DCM. Perforating the aluminium foil allows the initialization of the crystallization by the volatile DCM, which is a commonly used antisolvent for perovskite materials. The crystals of $MAPbBr_3$ and $DMA/MAPbBr_3$ are collected after 3-4 days on a filter paper and dried for 24 h in a vacuum oven kept at 40 °C.

Crystal characterizations: NMR (nuclear magnetic resonance) spectra were recorded on a Bruker Avance III spectrometer equipped with a Broad Band Inverse (BBI) probe. 16 transients were accumulated after an automatic 90° degree pulse optimization[72] without steady state scans, at 300 K, over a spectral width of 20.55 ppm (with a transmitter frequency offset at 6.18 ppm), at a fixed receiver gain (64), using 50 s of relaxation delay, (the acquisition time was 4.0 s). Free induction decay (FIDs) were apodized by using an exponential function equivalent to

0.3 Hz before Fourier transform. All the spectra were manually phased, automatically base line corrected and referred to the residual of not deuterated dimethyl sulfoxide (DMSO) signal calibrated at 2.50 ppm. Elemental analysis was performed via energy dispersive X-ray spectroscopy (EDS) on a JEOL JSM-7500FA SEM-Analytical field-emission scanning electron microscopy (SEM) with an Oxford X-Max 80 system equipped with an 80 mm^2 silicon drift detector (SDD). Laboratory X-ray powder diffraction (LXRPD) on the as-grown crystals and ground crystals was performed at room temperature (RT) using a PANalytical Empyrean X-ray diffractometer equipped with a 1.8 kW Cu Kα ceramic X-ray tube and a PIXcel^{3D} 2 × 2 area detector, operating at 45 kV and 40 mA. LXRPD data were analyzed using the HighScore 4.1 software from PANanalytical.[73] Step sizes of 0.013° and scan speeds of 0.013°/s were used for the scans, respectively. Temperature-dependent synchrotron X-ray powder diffraction (SXRPD) measurements in case of $MAPbBr_3$ and mixed DMA/$MAPbBr_3$ were carried out on sealed capillaries in transmission geometry at the Materials Science beamline of the Swiss Light Source,[74] using the Mythen III detector and a cryostream nitrogen blower to control the sample temperature. A 4 mm wide beam was employed, with a wavelength of 0.4923 Å calibrated against an NIST Si standard (SRM-640d). Room-temperature micro-Raman spectroscopy measurements were carried out in a Renishaw inVia instrument equipped with a 50× (0.75 N.A.) objective with an excitation wavelength of 785 nm. We checked a minimum of two crystals from different batches collecting spectra in 5-7 points for each sample. The temperature-dependent micro-Raman spectroscopy study was performed using a liquid nitrogen cryostat (Linkam) mounted in a Renishaw inVia microscope equipped with a long working distance objective (20×, 0.40 NA) with an excitation wavelength of 633 nm (non-resonant conditions to avoid PL signal contribution). We collected the Raman spectra in 5 different points for each sample. For all the Raman spectra acquisition a laser power < 1 mW was used to avoid the damage of the samples during the measurement. Absorbance measurements for the ground crystals were carried out on a Cary 5000 spectrometer equipped with a diffuse reflectance accessory. Ultraviolet photoelectron spectroscopy (UPS) analyses were performed on as-grown crystals with a Kratos Axis UltraDLD spectrometer, using a He I (21.22 eV) discharge lamp, on an area of 55 μm in diameter, at a pass energy of 10 eV and with a dwell time of 100 ms. The position of the valence band maximum (VBM) with respect to the vacuum level was estimated by measuring the width of the UPS spectra between the high- and low-binding energy intersections with the baseline, and subtracting the obtained value from the used photon energy. A -9.0 V bias was applied to the sample to precisely determine the high-binding-energy cutoff, as discussed by Helander and colleagues.[75] Temperature-dependent PL measurements were carried out on a FLS920 fluorescence spectrometer (Edinburgh instruments) coupled with optical fibres to collect the PL spectra. The crystals were attached to a sapphire substrate (TedPella®) with silver paste and placed inside a closed-cycle helium cryostat (Advanced Research Systems, Inc.) and the steady state PL spectra collected every 10 K using a 445 nm continuous wave (CW) Oxxius laser as excitation source placed in a reflecting geometry (45° between excitation and emission). The time-resolved PL measurements were carried using the 405 nm pulsed laser (50 ps) as an excitation source at a repetition rate of 0.5 MHz, to ensure complete decay of the emission between the excitation pulses. The PL decay traces were collected at the HE PL peak position with an emission bandwidth of 2 nm.

Photodetector device fabrication and characterization: For lateral devices, perovskite photodetectors were fabricated by depositing 60 nm thick Au electrodes via e-beam evaporation (using a Kenosistec® e-beam evaporator, equipped with a cooling system for the sample holder during evaporation) using a shadow mask (with a channel length of 50 µm and width of 1 mm), at a rate of 0.6 Å/s, resulting in an active area of a fabricated device of $A = 5 \times 10^{-4}$ cm^2. The sample was kept at 20 °C during the metal deposition to avoid any additional annealing effects. The dark IV curves and photocurrent responses were measured under vacuum using Keithley 2612 A source meter and a probe station from Janis Research® equipped with a closed-cycle

He cryogenic system. The measurements were controlled by a PC using LabView® software, and the bias voltage range between source and drain contacts was typically -2.5 to 2.5 V. The samples were illuminated with an optical fiber coupled to a white laser (NKT Photonics) whose wavelength was varied using an acoustic optic modulator from 500 to 650 nm. A calibrated Si photodetector from Thorlabs was used to measure the incident power, which was used to calculate the spectral responsivity (R). The detectivity can be derived from the noise equivalent power (NEP) and the active area of the photodetector A as:

$$D = \sqrt{A}/_{NEP}$$

and the NEP can be calculated from the thermal noise S_{th} and the shot noise S_S as follows

$NEP = \frac{S_{th}+S_S}{R}$,

Where the noise values are estimated by $S_{th} = \left(\frac{4\,kT}{V_D/I_D}\right)^{1/2}$, and $S_S = (2\,e\,I_D)^{1/2}$. Here V_D and I_D are the bias voltage of operation (1V) obtained and the related dark current (taken from the data reported in Figure 6), k is the Boltzmann constant, T is the temperature in Kelvin, and e the elementary charge.

Supporting Information

Supporting Information is available from the Wiley Online Library or from the author.

Acknowledgments

The authors thanks Dr. F. Baldassarre and R. Lassandro for their technical assistance and Dr. B.M. Aresta for the administrative support. B.M-G. thanks Gipuzkoa Council (Spain) in the frame of Gipuzkoa Fellows Program.

References

[1] J. S. Manser, M. I. Saidaminov, J. A. Christians, O. M. Bakr, P. V. Kamat, *Acc. Chem.*

Res. **2016**, *49*, 330.

[2] B. Saparov, D. B. Mitzi, *Chem. Rev.* **2016**, *116*, 4558.

[3] Y. Xu, Q. Lin, *Appl. Phys. Rev.* **2020**, *7*, 011315.

[4] M. Ahmadi, T. Wu, B. Hu, *Adv. Mater.* **2017**, *29*, 1.

[5] F. P. García De Arquer, A. Armin, P. Meredith, E. H. Sargent, *Nat. Rev. Mater.* **2017**, *2*, 1.

[6] J. Zhou, J. Huang, *Adv. Sci.* **2018**, *5*, DOI 10.1002/advs.201700256.

[7] J. Miao, F. Zhang, *J. Mater. Chem. C* **2019**, *7*, 1741.

[8] M. R. Filip, G. E. Eperon, H. J. Snaith, F. Giustino, *Nat. Commun.* **2014**, *5*, 1.

[9] A. Amat, E. Mosconi, E. Ronca, C. Quarti, P. Umari, M. K. Nazeeruddin, M. Grä, F. De Angelis, *Nano Lett* **2014**, *14*, 30.

[10] N. Shrestha, Z. Song, C. Chen, E. Bastola, X. Wang, Y. Yan, R. J. Ellingson, *J. Phys. Chem. Lett.* **2020**, *11*, 121.

[11] J. Shi, H. Zhang, Y. Li, J. J. Jasieniak, Y. Li, H. Wu, Y. Luo, D. Li, Q. Meng, *Energy Environ. Sci.* **2018**, *11*, 1460.

[12] J. Fu, N. F. Jamaludin, B. Wu, M. Li, A. Solanki, Y. F. Ng, S. Mhaisalkar, C. H. A. Huan, T. C. Sum, *Adv. Energy Mater.* **2019**, *9*, 1803119.

[13] A. D. Wright, R. L. Milot, G. E. Eperon, H. J. Snaith, M. B. Johnston, L. M. Herz, *Adv. Funct. Mater.* **2017**, *27*, 1700860.

[14] B. Yang, W. Ming, M.-H. H. Du, J. K. Keum, A. A. Puretzky, C. M. Rouleau, J. Huang, D. B. Geohegan, X. Wang, K. Xiao, *Adv. Mater.* **2018**, *30*, 1705801.

[15] T. Yin, Y. Fang, X. Fan, B. Zhang, J. L. Kuo, T. J. White, G. M. Chow, J. Yan, Z. X. Shen, *Chem. Mater.* **2017**, *29*, 5974.

[16] H. Ryu, H. R. Byun, K. M. McCall, D. Y. Park, T. J. Kim, M. S. Jeong, M. G. Kanatzidis, J. I. Jang, *J. Am. Chem. Soc.* **2021**, DOI 10.1021/jacs.0c11980.

[17] A. Francisco-López, B. Charles, M. I. Alonso, M. Garriga, M. T. Weller, A. R. Goñi,

Adv. Opt. Mater. **2021**, 2001969.

[18] E. M. Mozur, J. C. Trowbridge, A. E. Maughan, M. J. Gorman, C. M. Brown, T. R. Prisk, J. R. Neilson, *ACS Mater. Lett.* **2019**, *1*, 260.

[19] V. K. Sharma, R. Mukhopadhyay, A. Mohanty, M. Tyagi, J. P. Embs, D. D. Sarma, *J. Phys. Chem. Lett.* **2020**, *11*, 9669.

[20] M. Simenas, S. Balciunas, J. N. Wilson, S. Svirskas, M. Kinka, A. Garbaras, V. Kalendra, A. Gagor, D. Szewczyk, A. Sieradzki, M. Maczka, V. Samulionis, A. Walsh, R. Grigalaitis, J. Banys, *Nat. Commun.* **2020**, *11*, 1.

[21] S. Maheshwari, M. B. Fridriksson, S. Seal, J. Meyer, F. C. Grozema, *J. Phys. Chem. C* **2019**, *123*, 14652.

[22] S. Yesudhas, R. Burns, B. Lavina, S. N. Tkachev, J. Sun, C. A. Ullrich, S. Guha, *Phys. Rev. Mater.* **2020**, *4*, 105403.

[23] M. T. Weller, O. J. Weber, P. F. Henry, A. M. Di Pumpo, T. C. Hansen, *Chem. Commun.* **2015**, *51*, 4180.

[24] C. A. López, M. V. Martínez-Huerta, M. C. Alvarez-Galván, P. Kayser, P. Gant, A. Castellanos-Gomez, M. T. Fernández-Díaz, F. Fauth, J. A. Alonso, *Inorg. Chem.* **2017**, *56*, 14214.

[25] G. Saleh, G. Biffi, F. Di Stasio, B. Martín-García, A. L. Abdelhady, L. Manna, R. Krahne, S. Artyukhin, *Chem. Mater.* **2021**, acs. chemmater.1c03035.

[26] I. Spanopoulos, W. Ke, C. C. Stoumpos, E. C. Schueller, O. Y. Kontsevoi, R. Seshadri, M. G. Kanatzidis, *J. Am. Chem. Soc.* **2018**, *140*, 5728.

[27] D. J. Kubicki, D. Prochowicz, A. Hofstetter, M. Saski, P. Yadav, D. Bi, N. Pellet, J. Lewiński, S. M. Zakeeruddin, M. Grätzel, L. Emsley, *J. Am. Chem. Soc.* **2018**, *140*, 3345.

[28] C. Anelli, M. R. Chierotti, S. Bordignon, P. Quadrelli, D. Marongiu, G. Bongiovanni, L. Malavasi, *Inorg. Chem.* **2019**, *58*, 944.

[29] W. Ke, I. Spanopoulos, C. C. Stoumpos, M. G. Kanatzidis, *Nat. Commun.* **2018**, *9*, 1.

[30] W. M. J. Franssen, B. J. Bruijnaers, V. H. L. Portengen, A. P. M. Kentgens, *ChemPhysChem* **2018**, *19*, 3107.

[31] H. Chen, Q. Wei, M. I. Saidaminov, F. Wang, A. Johnston, Y. Hou, Z. Peng, K. Xu, W. Zhou, Z. Liu, L. Qiao, X. Wang, S. Xu, J. Li, R. Long, Y. Ke, E. H. Sargent, Z. Ning, *Adv. Mater.* **2019**, *31*, 1903559.

[32] W. M. J. Franssen, C. M. M. Van Heumen, A. P. M. Kentgens, *Inorg. Chem.* **2020**, *59*, 3730.

[33] G. E. Eperon, K. H. Stone, L. E. Mundt, T. H. Schloemer, S. N. Habisreutinger, S. P. Dunfield, L. T. Schelhas, J. J. Berry, D. T. Moore, G. E. Eperon, D. T. Moore, *ACS Energy Lett.* **2020**, *2020*, 1856.

[34] J. Shamsi, A. L. Abdelhady, S. Accornero, M. Arciniegas, L. Goldoni, A. R. S. Kandada, A. Petrozza, L. Manna, *ACS Energy Lett.* **2016**, *1*, 1042.

[35] K. M. Boopathi, B. Martín-garcía, A. Ray, J. M. Pina, S. Marras, M. I. Saidaminov, F. Bonaccorso, F. Di Stasio, E. H. Sargent, L. Manna, A. L. Abdelhady, M. Pina, S. Marras, M. I. Saidaminov, F. Bonaccorso, F. Di Stasio, E. H. Sargent, L. Manna, A. L. Abdelhady, *ACS Energy Lett.* **2020**, *5*, 642.

[36] A. Ray, B. Martín-García, A. Martinelli, D. Spirito, F. Locardi, D. Altamura, C. Giannini, M. Prato, L. Manna, A. L. Abdelhady, *J. Mater. Chem. A* **2020**, *8*, 17516.

[37] L. Kong, G. Liua, J. Gong, Q. Hu, R. D. Schaller, P. Dera, D. Zhang, Z. Liu, W. Yang, K. Zhu, Y. Tang, C. Wang, S. H. Wei, T. Xu, H. K. Mao, *Proc. Natl. Acad. Sci. U. S. A.* **2016**, *113*, 8910.

[38] A. Jaffe, Y. Lin, H. I. Karunadasa, *ACS Energy Lett.* **2017**, *2*, 1549.

[39] G. Liu, L. Kong, J. Gong, W. Yang, H. Mao, Q. Hu, Z. Liu, R. D. Schaller, D. Zhang, T. Xu, *Adv. Funct. Mater.* **2017**, *27*, 1604208.

[40] Y. Chen, Y. Lei, Y. Li, Y. Yu, J. Cai, M. H. Chiu, R. Rao, Y. Gu, C. Wang, W. Choi,

H. Hu, C. Wang, Y. Li, J. Song, J. Zhang, B. Qi, M. Lin, Z. Zhang, A. E. Islam, B. Maruyama, S. Dayeh, L. J. Li, K. Yang, Y. H. Lo, S. Xu, *Nature* **2020**, *577*, 209.

[41] K.-H. Wang, L.-C. Li, M. Shellaiah, K. Wen Sun, *Sci. Rep.* **2017**, *7*, 13643.

[42] E. M. Mozur, M. A. Hope, J. C. Trowbridge, D. M. Halat, L. L. Daemen, A. E. Maughan, T. R. Prisk, C. P. Grey, J. R. Neilson, *Chem. Mater.* **2020**, *32*, 6266.

[43] E. M. Mozur, A. E. Maughan, Y. Cheng, A. Huq, N. Jalarvo, L. L. Daemen, J. R. Neilson, *Chem. Mater* **2017**, *29*, 10168.

[44] A. Altomare, G. Campi, C. Cuocci, L. Eriksson, C. Giacovazzo, A. Moliterni, R. Rizzi, P. E. Werner, *J. Appl. Crystallogr.* **2009**, *42*, 768.

[45] F. Hao, C. C. Stoumpos, R. P. H. Chang, M. G. Kanatzidis, *J. Am. Chem. Soc.* **2014**, *136*, 8094.

[46] M. Keshavarz, M. Ottesen, S. Wiedmann, M. Wharmby, R. Küchler, H. Yuan, E. Debroye, J. A. Steele, J. Martens, N. E. Hussey, M. Bremholm, M. B. J. J. Roeffaers, J. Hofkens, *Adv. Mater.* **2019**, *31*, 1900521.

[47] P. S. Whitfield, N. Herron, W. E. Guise, K. Page, Y. Q. Cheng, I. Milas, M. K. Crawford, *Sci. Rep.* **2016**, *6*, 1.

[48] E. M. Mozur, J. R. Neilson, *Annu. Rev. Mater. Res.* **2021**, *51*, DOI 10.1146/annurev-matsci-080819-012808.

[49] M. Mączka, M. Ptak, *Appl. solid state Chem.* **2018**, *1*, 45.

[50] B. Martín-García, D. Spirito, G. Biffi, S. Artyukhin, Francesco Bonaccorso, R. Krahne, *J. Phys. Chem. Lett.* **2021**, *12*, 280.

[51] A. M. A. Leguy, A. R. Goñi, J. M. Frost, J. Skelton, F. Brivio, X. Rodríguez-Martínez, O. J. Weber, A. Pallipurath, M. I. Alonso, M. Campoy-Quiles, M. T. Weller, J. Nelson, A. Walsh, P. R. F. Barnes, *Phys. Chem. Chem. Phys.* **2016**, *18*, 27051.

[52] M. D. Hanwell, D. E. Curtis, D. C. Lonie, T. Vandermeerschd, E. Zurek, G. R. Hutchison, *J. Cheminform.* **2012**, *4*, 17.

[53] W. Kong, Z. Ye, Z. Qi, B. Zhang, M. Wang, A. Rahimi-Iman, H. Wu, *Phys. Chem. Chem. Phys.* **2015**, *17*, 16405.

[54] F. Panzer, S. Baderschneider, T. P. Gujar, T. Unger, S. Bagnich, M. Jakoby, H. Bässler, S. Hüttner, J. Köhler, R. Moos, M. Thelakkat, R. Hildner, A. Köhler, *Adv. Opt. Mater.* **2016**, *4*, 917.

[55] C. Wehrenfennig, M. Liu, H. J. Snaith, M. B. Johnston, L. M. Herz, *APL Mater.* **2014**, *2*, 081513.

[56] B. Wu, H. Yuan, Q. Xu, J. A. Steele, D. Giovanni, P. Puech, J. Fu, Y. F. Ng, N. F. Jamaludin, A. Solanki, S. Mhaisalkar, N. Mathews, M. B. J. Roeffaers, M. Grätzel, J. Hofkens, T. C. Sum, *Nat. Commun.* **2019**, *10*, 1.

[57] J. A. Steele, P. Puech, B. Monserrat, B. Wu, R. X. Yang, T. Kirchartz, H. Yuan, G. Fleury, D. Giovanni, E. Fron, M. Keshavarz, E. Debroye, G. Zhou, T. C. Sum, A. Walsh, J. Hofkens, M. B. J. Roeffaers, *ACS Energy Lett.* **2019**, *4*, 2205.

[58] H. Ryu, D. Y. Park, K. M. McCall, H. R. Byun, Y. Lee, T. J. Kim, M. S. Jeong, J. Kim, M. G. Kanatzidis, J. I. Jang, *J. Am. Chem. Soc.* **2020**, *142*, 21059.

[59] M. I. Dar, G. Jacopin, S. Meloni, A. Mattoni, N. Arora, A. Boziki, S. M. Zakeeruddin, U. Rothlisberger, M. Grätzel, *Sci. Adv.* **2016**, *2*, e1601156.

[60] J. M. Frost, K. T. Butler, F. Brivio, C. H. Hendon, M. Van Schilfgaarde, A. Walsh, *Nano Lett.* **2014**, *14*, 2584.

[61] H. C. Woo, J. W. Choi, J. Shin, S. H. Chin, M. H. Ann, C. L. Lee, *J. Phys. Chem. Lett.* **2018**, *9*, 4066.

[62] L. Zhao, Y. Gao, M. Su, Q. Shang, Z. Liu, Q. Li, Q. Wei, M. Li, L. Fu, Y. Zhong, J. Shi, J. Chen, Y. Zhao, X. Qiu, X. Liu, N. Tang, G. Xing, X. Wang, B. Shen, Q. Zhang, *ACS Nano* **2019**, *13*, 10085.

[63] F. Panzer, C. Li, T. Meier, A. Köhler, S. Huettner, *Adv. Energy Mater.* **2017**, *7*, 1700286.

[64] S. Singh, C. Li, F. Panzer, K. L. Narasimhan, A. Graeser, T. P. Gujar, A. Köhler, M. Thelakkat, S. Huettner, D. Kabra, *J. Phys. Chem. Lett.* **2016**, *7*, 3014.

[65] A. Francisco-López, B. Charles, O. J. Weber, M. I. Alonso, M. Garriga, M. Campoy-Quiles, M. T. Weller, A. R. Goñi, *J. Phys. Chem. Lett.* **2019**, *10*, 2971.

[66] A. Rubino, A. Francisco-López, A. J. Barker, A. Petrozza, M. E. Calvo, A. R. Goñi, H. Míguez, *J. Phys. Chem. Lett.* **2020**, *12*, 569.

[67] H. Zhu, K. Miyata, Y. Fu, J. Wang, P. P. Joshi, D. Niesner, K. W. Williams, S. Jin, X. Y. Zhu, *Science* **2016**, *353*, 1409.

[68] K. Miyata, T. L. Atallah, X.-Y. Y. Zhu, *Sci. Adv.* **2017**, *3*, e1701469.

[69] A. Osherov, E. M. Hutter, K. Galkowski, R. Brenes, D. K. Maude, R. J. Nicholas, P. Plochocka, V. Bulović, T. J. Savenije, S. D. Stranks, *Adv. Mater.* **2016**, *28*, 10757.

[70] K. Higgins, M. Lorenz, M. Ziatdinov, R. K. Vasudevan, A. V. Ievlev, E. D. Lukosi, O. S. Ovchinnikova, S. V. Kalinin, M. Ahmadi, *Adv. Funct. Mater.* **2020**, *30*, 2001995.

[71] D. W. Ferdani, S. R. Pering, D. Ghosh, P. Kubiak, A. B. Walker, S. E. Lewis, A. L. Johnson, P. J. Baker, M. S. Islam, P. J. Cameron, *Energy Environ. Sci.* **2019**, *12*, 2264.

[72] P. S. C. Wu, G. Otting, *J. Magn. Reson.* **2005**, *176*, 115.

[73] T. Degen, M. Sadki, E. Bron, U. König, G. Nénert, in *Powder Diffr.*, Cambridge University Press, **2014**, pp. S13–S18.

[74] P. R. Willmott, D. Meister, S. J. Leake, M. Lange, A. Bergamaschi, M. Böge, M. Calvi, C. Cancellieri, N. Casati, A. Cervellino, Q. Chen, C. David, U. Flechsig, F. Gozzo, B. Henrich, S. Jäggi-Spielmann, B. Jakob, I. Kalichava, P. Karvinen, J. Krempasky, A. Lüdeke, R. Lüscher, S. Maag, C. Quitmann, M. L. Reinle-Schmitt, T. Schmidt, B. Schmitt, A. Streun, I. Vartiainen, M. Vitins, X. Wang, R. Wullschleger, *J. Synchrotron Radiat.* **2013**, *20*, 667.

[75] M. G. Helander, M. T. Greiner, Z. B. Wang, Z. H. Lu, *Appl. Surf. Sci.* **2010**, *256*, 2602.

TOC

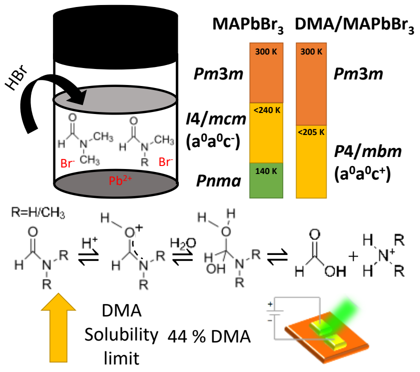
HBr
Br⁻
Pb²⁺
Br⁻
MAPbBr₃
DMA/MAPbBr₃
Pm3m
300 K
300 K
Pm3m
I4/mcm
(a⁰a⁰c⁻)
<240 K
<205 K
P4/mbm
(a⁰a⁰c⁺)
140 K
Pnma
R=H/CH₃
H⁺
H₂O
DMA
Solubility
limit
44 % DMA